*Article*

# Enhanced Plasmonic Photocatalysis of Au-Decorated ZnO Nanocomposites

**Maria Stefan** [1], **Adriana Popa** [1], **Dana Toloman** [1], **Cristian Leostean** [1], **Lucian Barbu-Tudoran** [1,2] **and Alexandra Falamas** [1,*]

[1] National Institute for Research and Development of Isotopic and Molecular Technologies, 67-103 Donat, 400293 Cluj-Napoca, Romania; maria.stefan@itim-cj.ro (M.S.); adriana.popa@itim-cj.ro (A.P.); dana.toloman@itim-cj.ro (D.T.); cristian.leostean@itim-cj.ro (C.L.); lucian.barbu@itim-cj.ro (L.B.-T.)

[2] Electron Microscopy Laboratory "Prof. C. Craciun", Faculty Biology & Geology, Babes-Bolyai University, 5-7 Clinicilor St., 400006 Cluj-Napoca, Romania

[*] Correspondence: alexandra.falamas@itim-cj.ro

**Abstract:** The rapid development of technological processes in various industrial fields has led to surface water pollution with different organic pollutants, such as dyes, pesticides, and antibiotics. In this context, it is necessary to find modern, environmentally friendly solutions to avoid the hazardous effects on the aquatic environment. The aim of this paper is to improve the photocatalytic performance of zinc oxide (ZnO) nanoparticles by using the plasmonic resonance induced by covering them with gold (Au) nanoparticles. Therefore, we evaluate the charge carriers' behavior in terms of optical properties and reactive oxygen species (ROS) generation. The ZnO-Au nanocomposites were synthesized through a simple chemical protocol in multiple steps. ZnO nanoparticles (NPs) approximately 20 nm in diameter were prepared by chemical precipitation. ZnO-Au nanocomposites were obtained by decorating the ZnO NPs with Au at different molar ratios through a reduction process. X-ray diffraction (XRD) analysis and transmission electron microscopy (TEM) confirmed the simultaneous presence of hexagonal ZnO and cubic Au phases. The optical investigations evidenced the existence of a band-gap absorption peak of ZnO at 372 nm, as well as a surface plasmonic band of Au nanoparticles at 573 nm. The photocatalytic tests indicated increased photocatalytic degradation of the Rhodamine B (RhB) and oxytetracycline (OTC) pollutants under visible light irradiation in the presence of ZnO-Au nanocomposites (60–85%) compared to ZnO NPs (43%). This behavior can be assigned to the plasmonic resonance and the synergetic effects of the individual constituents in the composite nanostructures. The spin-trapping experiments showed the production of ROS while the nanostructures were in contact with the pollutants. This study introduces new strategies to adjust the efficiency of photocatalytic devices by the combination of two types of nanostructures with synergistic functionalities into one single entity. ZnO-Au nanocomposites can be used as stable photocatalysts with excellent reusability and possible industrial applications.

**Keywords:** ZnO-Au nanocomposites; surface plasmon resonance; plasmon photocatalysis; reactive oxygen species

## 1. Introduction

The rapid development of technological processes in various industrial fields has led to surface water pollution with different organic pollutants, such as dyes, pesticides, antibiotics, and other organic compounds [1–8]. Numerous studies have suggested hazardous effects on human health and the environment [7,8]. In this context, it is necessary to find modern, environmentally friendly solutions to avoid the hazardous effects to the aquatic environment [8]. Zinc oxide is one of the most studied multifunctional materials [9–11] by virtue of its availability, physical and chemical stability, low synthesis costs, and biocompatibility, being used in an increasing number of industrial applications [12–17]. It

is an n-type semiconductor with a high bandgap energy (3.37 eV), high coupling energy (60 meV), and high thermal and mechanical stability. From this point of view, ZnO is widely used in wastewater depollution technologies for the purpose of sustaining the quality of human life and the global environment [18–20]. Semiconductor-based photocatalysis is known as a sustainable and green advanced oxidation process (AOP) technology capable of solving water-related environmental issues [21–24]. In such systems, the behavior of charge carriers is strongly related to the reactivity of photogenerated electrons and holes, a process dependent on the surface structure of materials [25,26].

An important role in the photocatalytic processes is represented by reactive oxygen species (ROS), strong oxidizing agents formed at the liquid/photocatalyst interface [27,28] in the presence of charge carriers, which have the advantage of rapidly degrading a wide range of recalcitrant pollutants, even at low concentrations. In photocatalytic applications, the use of solar light is necessary in order to avoid using other light sources that involve additional costs. Considering the specificity of UV radiation absorption by ZnO photocatalysts, which represents only 5% of the solar light spectrum, much research has aimed at modulating their spectral response in the visible region [29–31]. Among various strategies, it has been shown that noble metal coupling can be used to fine-tune and even amplify the optical properties of ZnO nanoparticles [32] due to the resulting localized surface plasmon resonance (LSPR) [33,34]. ZnO–metal nanocomposites can be easily configured in various shapes, either by growing or attaching metal NPs onto the surface of previously synthesized ZnO nanostructures. Various techniques have been investigated, including depositing gold on ZnO nanostructures using pulsed laser deposition [35], sputtering [36,37], microwave-assisted chemical synthesis [38], and chemical reduction [39,40]. Of these, the chemical reduction of gold to obtain ZnO-Au nanocomposites is a simple method that does not require sophisticated equipment or high energy consumption. Metal–semiconductor plasmonic nanocomposites have been developed in various configurations, such as core–shell nanostructures [40], metal-incorporated semiconducting surfaces, and metal supported on semiconducting surfaces [35,36].

The specific combination of different components into nanocomposites, in this case ZnO and noble metals, can facilitate charge transportation and reduce electron–hole recombination, thus increasing the photocatalytic response [41,42]. Accordingly, modulating the surface structure of semiconductors' nanocomposites can optimize their charge carrier behavior, which is responsible for high photocatalytic efficiency. Data in the literature have reported the photocatalytic properties of different metal oxides interfaced with noble metal nanocomposites for the removal of various dyes, such as rhodamine B, methylene blue, and rhodamine 6G [1–3], as well as other pollutants, including 4-nitrophenol [4], nitrogen oxides [5], and antibiotics [6–8]. Other studies related to the photocatalytic removal of dyes from aqueous environments have shown efficiencies of degradation ranging from 45% to 100%, depending on the time of visible light irradiation [43–46]. It is worth mentioning here that most papers assessed the general assets of the photocatalytic process using high concentrations of pollutants without any details regarding ROS or core–shell defects, which are critical factors in the photocatalytic mechanism.

Within the above context, this study presents a complex investigation of ZnO-Au photocatalysts for the photo-degradation of RhB and OTC pollutants. The novelty of this paper is due to the fabrication of ZnO-Au nanocomposites using a simple and fast chemical synthesis route, and to the improved photocatalytic activity obtained for ZnO NPs by modulating their spectral response through Au decoration. Detailed investigations into the photocatalytic properties of the obtained nanocomposites were analyzed regarding ROS generation, which led to the degradation of the organic molecules RhB and OTC. Furthermore, the presence of core–shell defects, revealed by EPR spectroscopy, was able to tailor the e−/h+ recombination as a function of the Au content. The motivation for choosing Au-decorated ZnO nanocomposites was strongly related to their unique properties. The LSPR induced by the Au nanoparticles decorating the ZnO surface is one of the main strategies to modify the spectral response of ZnO photocatalysts toward visible light (solar

light). Therefore, the advantage of using sunlight as a green and inexhaustible energy source for the degradation of harmful pollutants in wastewater, as well as the increased photocatalytic performance of the ZnO-Au nanocomposites, can exceed the disadvantage posed by the price of gold. Considering the above, the aim of the proposed nanocomposites was to increase the photocatalytic performance using low doses of photocatalysts, low pollutant concentrations, and low energy consumption.

## 2. Results and Discussion

Considering that the choice of synthesis method and the rigorous control of the experimental parameters largely influence the design of a material with targeted properties, we focused on some particular aspects regarding the synthesis of ZnO-Au nanocomposites. The synthesis of ZnO-Au nanoparticles was performed following two sequential steps, aiming for the formation of a heterojunction. At the beginning, ZnO nanoparticles were obtained by chemical precipitation. In the next step, decoration of ZnO nanoparticles' surfaces with Au was performed by a reduction of gold precursor in the presence of hydrazine. The following reactions were proposed as evidence for the composite formation (1)–(4):

$$Zn(CH_3COO)_2 + NaOH^+ \rightarrow Zn(OH)_2 + 2CH_3COONa \tag{1}$$

$$Zn(OH)_2 + 2OH^- \rightarrow [Zn(OH)_4]^- \tag{2}$$

$$Zn(OH)_2 \rightarrow ZnO + H_2O \tag{3}$$

$$4HAuCl_4 + 3N_2H_4 \rightarrow 4Au + 3N_2\uparrow + 16HCl \tag{4}$$
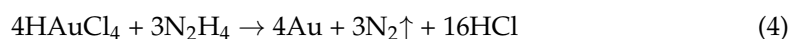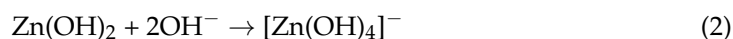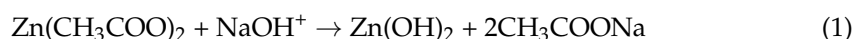
Figure 1 presents a scheme of the steps used for synthesizing the ZnO-Au nanocomposites. To highlight the properties of ZnO-Au nanocomposites, a series of three samples was prepared, namely, ZnO, ZnO-Au1, and ZnO-Au2, which differ with respect to the quantity of Au in the composite sample.
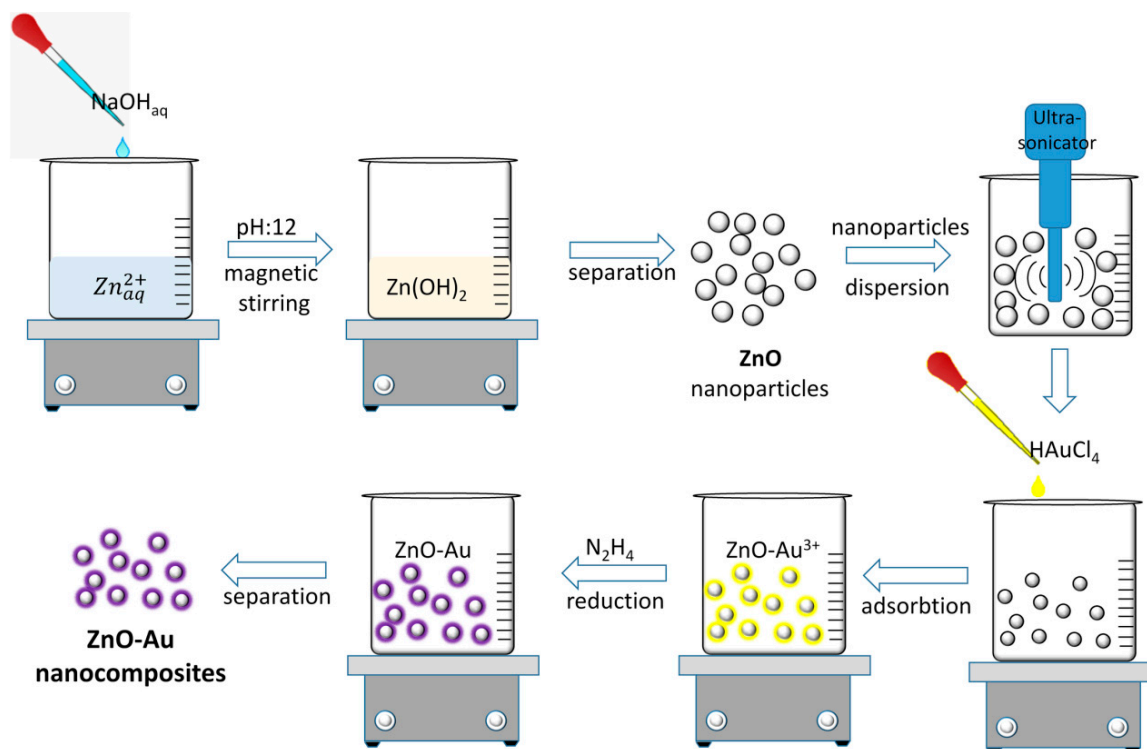


**Figure 1.** Schematic representation of the synthesis steps for obtaining ZnO-Au nanocomposites.

### 2.1. Structural, Morphological, and Thermal Properties

The structural characterization of ZnO and ZnO-Au nanocomposites is revealed in Figure 2. For ZnO nanoparticles, the diffraction planes (100), (002), (101), (102), (110), (103), (112), (201), and (100) of hexagonal ZnO (PDF card 99-100-4548) were identified. No other peaks related to possible impurities were observed. The characteristic diffraction peaks of the ZnO sample were broad, indicating that the crystallites were in nanometric scale. The lattice parameters were a = 3.2515 Å; b = 3.2515 Å, c = 5.203, and the unit cell volume was 47.52 Å. Furthermore, the diffraction planes (111), (200), and (311) of cubic Au (PDF File 00-001-1172) were observed in the ZnO-Au samples. The width of the peak suggested the nanocrystalline character of gold, and increased with the gold content. The XRD data were in good agreement with results obtained by others [38,41]. These results suggest the occurrence of heterojunction formation between ZnO and Au to obtain ZnO-Au nanocomposites.
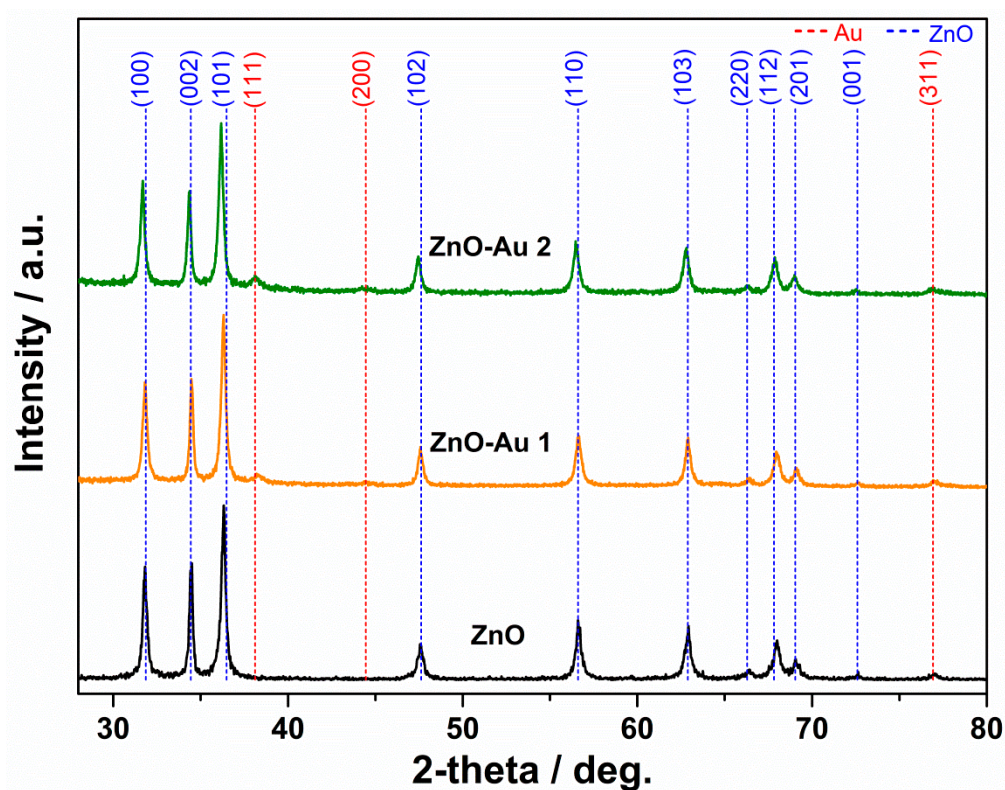


**Figure 2.** X-ray diffraction data characteristics of the ZnO nanoparticles and the ZnO-Au nanocomposites.

Powder Cell 2.3 software and the Williamson–Hall plot [47] were employed to estimate the mean size of the crystallites, (<D>), for both the zinc oxide and the gold phases. In Table 1, the synthetic details are given for both the ZnO NPs and the ZnO-Au nanocomposites, together with the dimensions of the crystallites obtained from the diffraction data.

**Table 1.** The synthetic details and crystallite size for the pure ZnO nanoparticles and the ZnO-Au nanocomposites.

| Sample | Molar Ratio ZnO:Au | Crystallites Dimension (nm) | |
|---|---|---|---|
| | | ZnO | Au |
| ZnO | 1:0 | 21.8 | - |
| ZnO-Au1 | 1:3 | 35.0 | 14.5 |
| ZnO-Au2 | 1:4 | 32.1 | 19.2 |

The TEM images clearly revealed the Au nanoparticles on the surface of the ZnO nanostructures (Figure 3). The images showed ZnO nanoparticles of various polyhedral shapes that tend to aggregate. The particles' size distribution demonstrated that ~18 nm ZnO nanoparticles were decorated with ~7 nm spherical Au nanoparticles randomly distributed on the surfaces of the ZnO nanoparticles. The dispersal of the relative volumes as a function of diameter was further investigated in order to correlate the TEM and XRD results [48]. One can see that most of the nanostructures showed peaks around 20 and 33 nm, in accordance with the mean diameter obtained from XRD investigations. Additionally, the EDX analysis allowed us to determine the elemental composition of ZnO-Au nanocomposites. The results are given in Table 2.
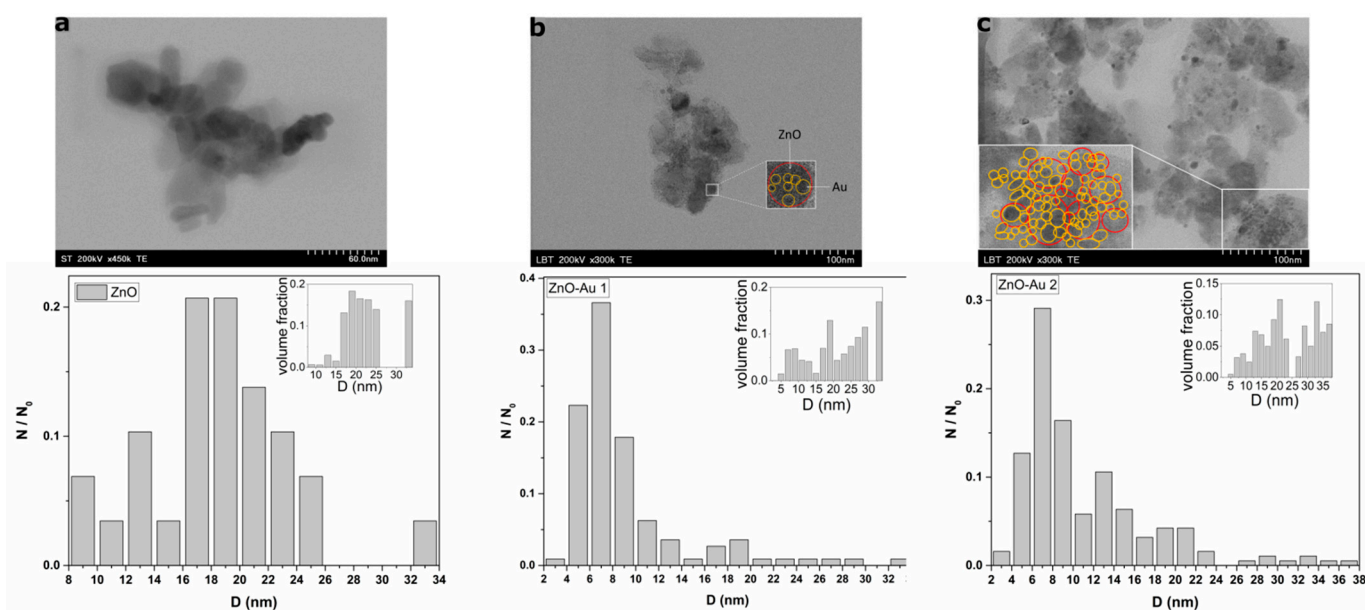


**Figure 3.** TEM images representing the ZnO nanoparticles (**a**) and the ZnO-Au nanocomposites (ZnO-Au1—(**b**) and ZnO-Au2—(**c**)), together with their corresponding sizes and volume fraction distributions.

**Table 2.** Elemental composition of ZnO-Au nanocomposites determined through EDX analysis.

| Sample | Zn (wt%) | O (wt%) | Au (wt%) |
|---|---|---|---|
| ZnO | 49.2 | 50.8 | - |
| ZnO-Au1 | 52.4 | 45.8 | 1.8 |
| ZnO-Au2 | 51.9 | 45.6 | 2.5 |

The elemental distribution was evaluated by EDX mapping (Figure 4), and it showed that the samples contained only Zn, Au and O, revealing the absence of any impurities.

XPS investigations revealed the surface elemental composition of the ZnO-Au nanocomposites. The Zn *2p* core-level spectrum is shown in Figure 5a. The $Zn^{2+}$ from the ZnO lattice was evidenced by the *2p* (3/2) and *2p* (1/2) peaks which were positioned at 1021.64 and 1044.74 eV. The Au *4f* and Zn *2p* core-level deconvoluted spectra are shown in Figure 5b. The Zn *2p* (3/2) and *2p* (1/2) peaks were positioned at 87.85 and 90.85 eV, while the Au *4f* (7/2) and *4f* (5/2) peaks were positioned at 83.29 and 86.99 eV. The observed 83.29 eV Au *4f* (7/2) peak position was lower than the expected 84 eV. This is evidence of a negative charge on the Au nanoparticles' surfaces [49].
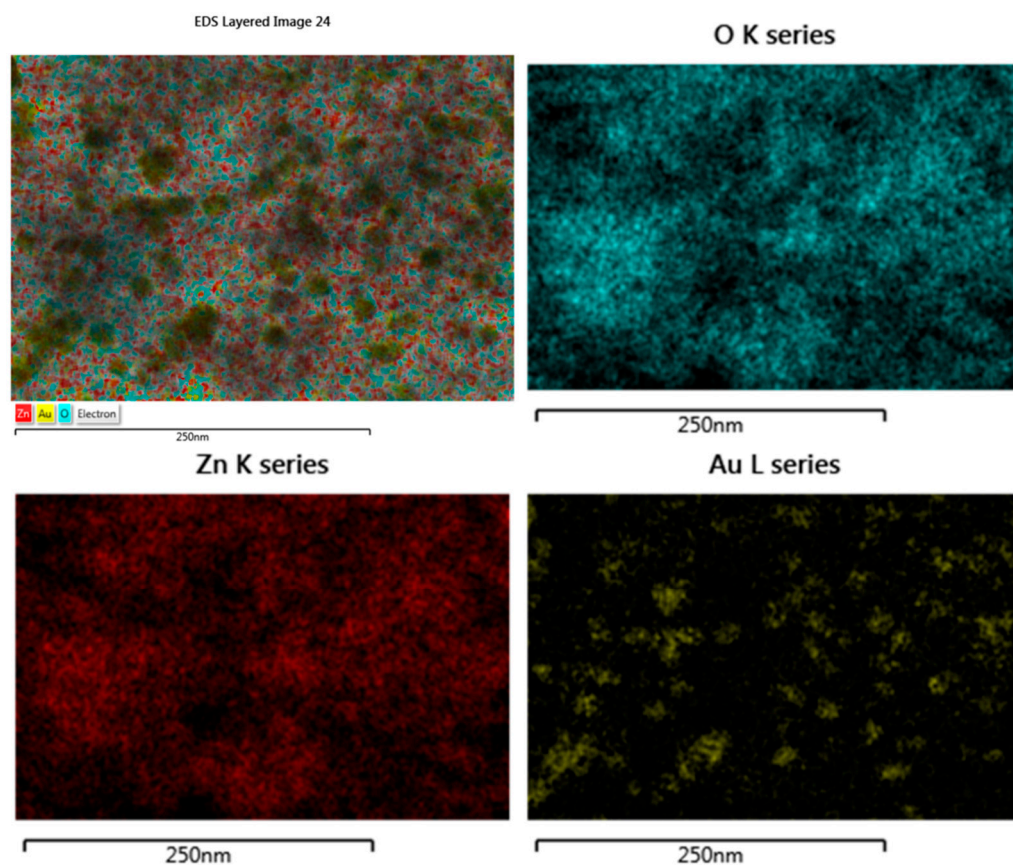
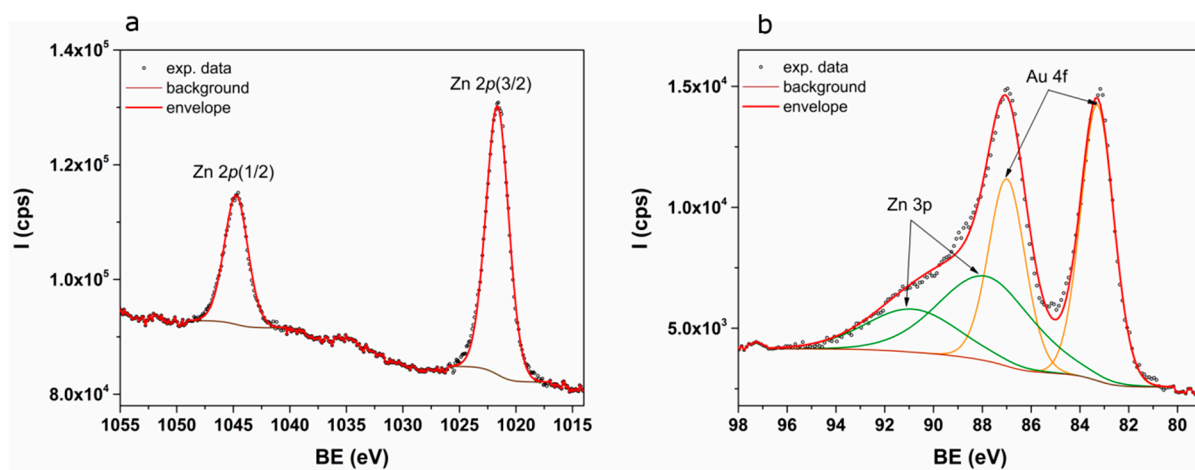**Figure 4.** The EDS mapping of the ZnO-Au2 nanocomposites.



**Figure 5.** XPS spectra of core-level lines, corresponding to Zn *2p* (**a**) and Au *4f* and Zn *3p* (**b**).

The XPS elemental depth profile analysis was performed using Ar ions etching at 1500 V acceleration voltage and 10 mA filament current. Figure 6 shows that the Au *4f* (7/2) intensity decreased, while the intensity Zn *2p* (3/2) remained constant. This result indicates a core–shell-like/decorated structure. The relative constant intensity of Zn can be explained by taking into account that the theoretical sputter depth for 1500 V is ~1.8 nm/h. Thus, the total sputtering time of ~2 h provided data up to ~3.6 nm.
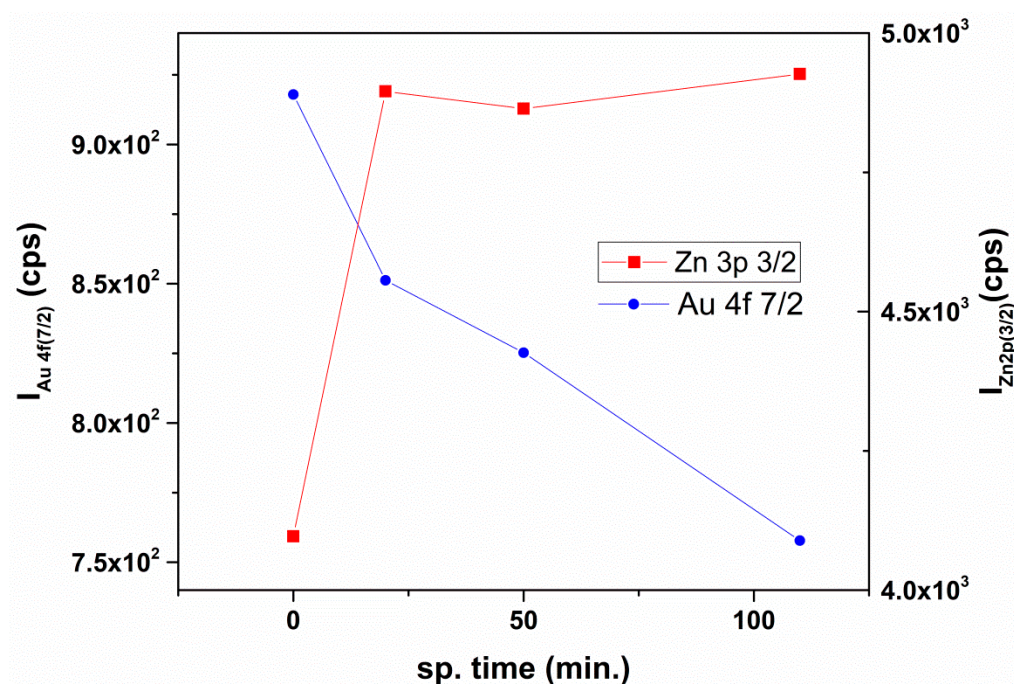
**Figure 6.** Comparative variation of XPS Au *4f* (7/2) and Zn *2p* (3/2) core–level line intensities assigned to ZnO-Au2 as a function of the etching time.

Further, the optical properties characteristic of the ZnO-Au nanocomposites were investigated. The aim was to provide evidence for the effect of the plasmon band on the properties of ZnO NPs. Figure 7 presents the UV-Vis absorption spectra characteristic of the ZnO-Au nanocomposites in comparison to those of the ZnO NPs used for Au decoration.
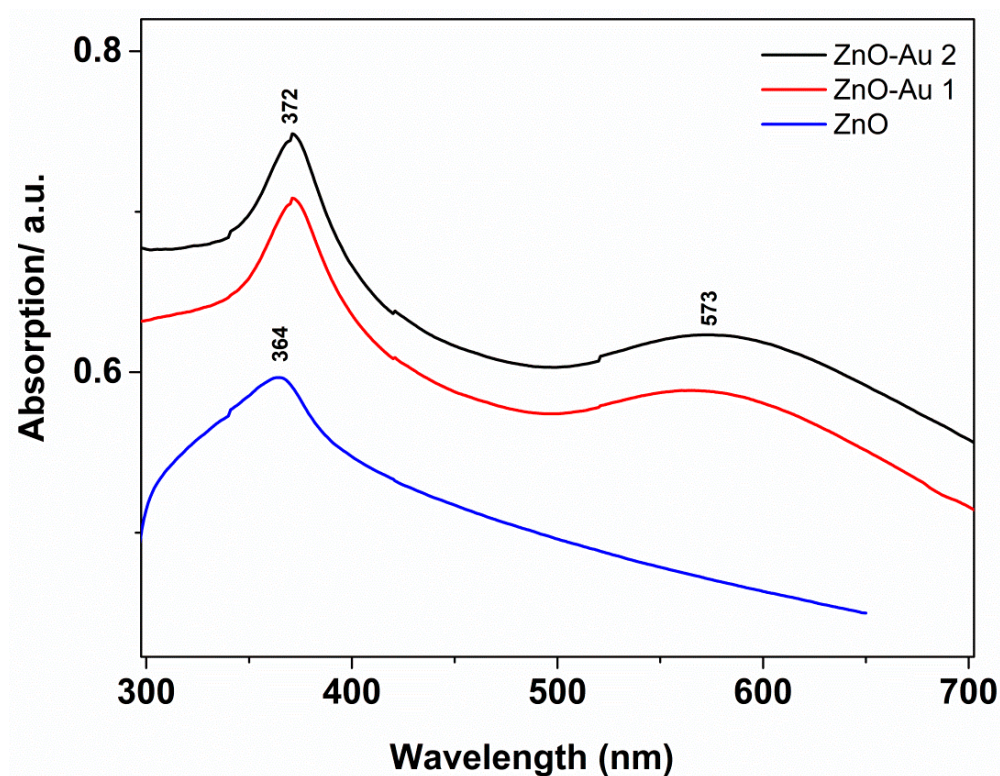


**Figure 7.** UV-Vis spectra acquired from ZnO nanoparticles and the ZnO-Au nanocomposites, respectively.

The UV-Vis absorption spectrum corresponding to the ZnO NPs showed a sharp band-gap absorption peak characteristic of ZnO at 364 nm. The presence of Au NPs slightly shifted the absorption peak towards higher wavelengths at 372 nm due to the interfacial heterojunction between Au and ZnO. Additionally, in ZnO-Au samples, the LSPR band of the Au NPs was detected in the visible spectral range, around 575 nm, as a well-developed absorption band, which further confirms the presence of Au nanoparticles in the ZnO-Au nanocomposites. The LSPR band covered most of the visible absorption spectral region [38,50].

The fluorescence spectra given in Figure 8 indicate the effect that the Au decoration had on the emission properties of ZnO nanoparticles. The fluorescence spectra specific to the pure ZnO NPs showed a dominant UV emission, followed by medium- to low-intensity visible emissions. The free exciton recombination peak was observed around 380 nm, and lower-intensity visible emission peaks were located at 470 and 545 nm, respectively, corresponding to defects in the vacancy levels of oxygen and zinc.
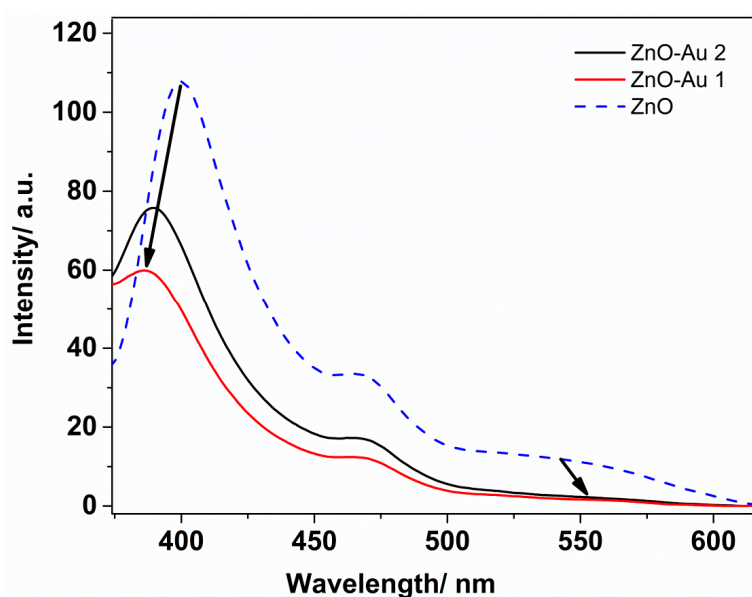


**Figure 8.** Fluorescence spectra characteristic of the ZnO nanoparticles and the ZnO-Au nanocomposites. Excitation: 340 nm.

Compared with the standalone ZnO nanoparticles, a blue-shifting of the emission peaks specific to ZnO-Au nanocomposites was observed, in addition to intensity quenching. This behavior occurred because the Au nanoparticles in contact with the ZnO surface repressed the recombination of photo-generated electrons and holes [3,51]. On the other hand, the defects resulting from the nucleation of Au nanoparticles were able to trap the photogenerated species due to surface passivation, resulting in luminescence quenching. These properties stimulated the generation of ROS, which conferred to our ZnO-Au nanocomposites the property to act as efficient photocatalysts. As shown in Figure 8, the blue-shift of UV emission was assigned to the interfacial charge transfer between ZnO and Au NPs. Moreover, the transfer of the charge carrier at the interface determined the quenching of ZnO emission [52].

In order to identify the possible defects in ZnO nanoparticles and ZnO-Au nanocomposites, the EPR spectra (Figure 9) were recorded. The resonance signals observed in Figure 9a, one located at g = 1.96 and the other at g = 2.006, indicate the presence of defective states in all samples. According to the data from the literature, the provenience of the first signal (g = 1.96) can be assigned to ionized oxygen vacancy $V_0^+$ [53], shallow donors [54], free electrons [55], or core defect signals when the core–shell framework is considered [56]. Recent findings related to defective centers at the surface of the nanoparticles have evidenced different origins for the second signal (g = 2.006), such as trapped hole

centers, oxygen vacancies [54], zinc vacancies, or chemisorbed oxygen [57]. Considering that the integral intensity of the resonance signal is dependent on the number of spins participating in resonance, the intensities of the aforementioned resonance signals were calculated, and the results are shown in Figure 9b. The dependence of the integrated intensities on the amount of Au used for decorating the ZnO nanostructures suggests that the core defects were diminished and the shell defects remained constant with the increasing Au content in the final sample. Thus, it can be stated that the ZnO lattice is reorganized during the reduction in $HAuCl_4$ precursor.
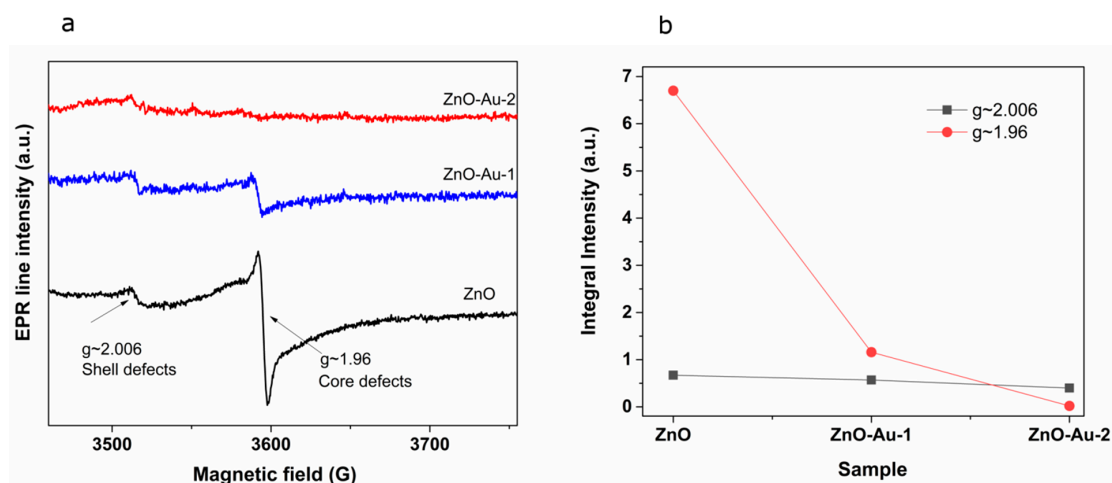


**Figure 9.** EPR spectra of ZnO nanoparticles and ZnO-Au nanocomposites (**a**); the integral intensity of the resonance signal (**b**).

Furthermore, the thermal stability of the ZnO-Au nanocomposites was analyzed. When these nanocomposites are used in photocatalytic applications, any change in the composition of the sample or undesirable phase transformation with temperature is very important for obtaining the desired photocatalytic efficiency. In Figure 10, the thermal behavior (thermogravimetric (TG); differential thermal analysis (DTA); and derivative thermogravimetric (DTG) curves) of ZnO-Au1 nanocomposites is illustrated.
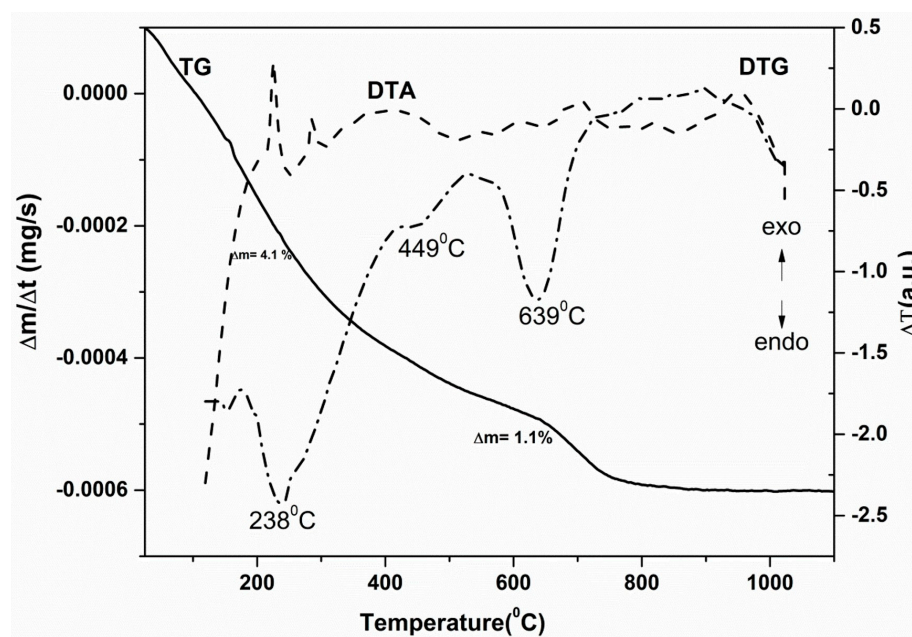


**Figure 10.** TG, DTA, and DTG curves of ZnO-Au1 nanocomposites.

In the temperature range of 25–550 °C, the ZnO-Au nanocomposites showed a progressive mass loss of 4.1%, mainly due to vaporization, surface dihydroxylation, and removal of solvents; these processes are associated with a small and wide endothermic peak at 180 °C. The oxidation and combustion of certain parts of ZnO-Au nanocomposites took place between 550–900 °C, with a small weight loss of ~1%. This thermal process determined a small exothermic peak in the DTA curves of nanocomposites registered at 780 °C. A structural disorder related to oxygen release from the ZnO lattice was evidenced to reach up to 900 °C, with exothermic effects in the DTA curves [58]. Since the synthesis of such nanocomposites requires temperatures up to 450 °C to obtain highly crystalline ZnO nanocomposites, the thermal processes that took place above this temperature can be neglected. Taking into account these observations, ZnO-Au nanocomposites can be used as stable thermal photocatalysts.

### 2.2. Photocatalytic Properties

The ability of ZnO-Au nanocomposites to serve as photocatalysts was proven through the degradation of Rhodamine B and oxytetracycline pollutants. For comparison, the ZnO nanoparticles were tested as well. Prior to the photocatalytic process, the adsorption of RhB and OTC on the surface of ZnO and ZnO-Au nanocomposites was tested in the dark. The results showed that the adsorption–desorption equilibrium was reached after 60 min. After that, the mixture was irradiated by visible light, and the absorption of RhB versus irradiation time was monitored. The decrease of intensity in the absorption peak, corresponding to RhB in the presence of ZnO-Au1, is shown in the inset in Figure 11a at different time intervals. The photocatalytic degradation of RhB and OTC in the presence of ZnO-Au1, ZnO-Au2, and ZnO nanostructures was calculated using Equation (5), and is given in Figure 11. After 300 min of visible light irradiation, the percentage of RhB dye degradation was as follows: ZnO-Au1 (85%), ZnO-Au2 (60%), and ZnO (43%). In the case of OTC, the photocatalytic activity was calculated based on the absorption band centered at 375 nm. The results show that ZnO-Au1 exhibited the best degradation (63%), followed by ZnO-Au2 (37%) and ZnO (29%). In conclusion, the Au decoration of the ZnO nanostructures increased the photocatalytic activity of the pure ZnO samples.
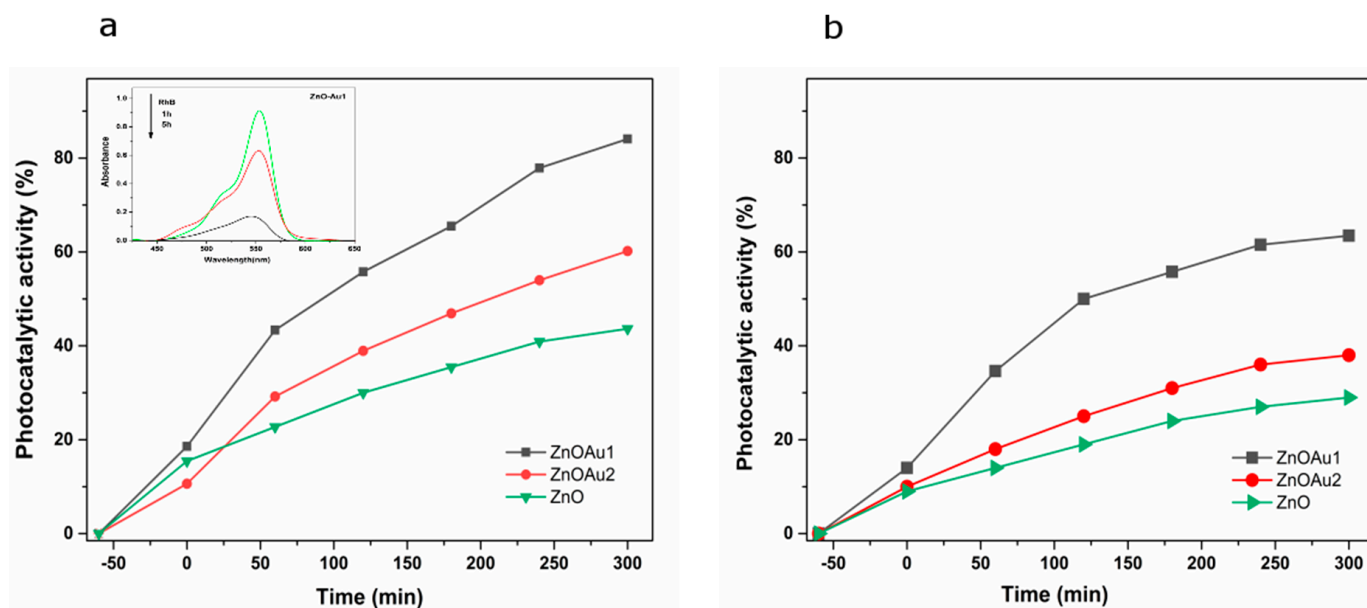


**Figure 11.** Photocatalytic degradation of (**a**) RhB and (**b**) OTC in the presence of ZnO nanoparticles: respectively, ZnO-Au1 and ZnO-Au2 nanocomposites. The inset in (**a**) represents the UV-vis absorption spectra of RhB aqueous solution in the presence of ZnO-Au1 at different irradiation time intervals.

The photocatalytic activity was described through the first-order kinetic model (Equation (6)), and a linear fitting of the obtained data as a function of the irradiation time was detected (Figure 12). The resulting $k_i$ values and the correlation coefficient $R^2$ indicate that the ZnO-Au1 photocatalyst presented the best photocatalytic activity for both pollutants.
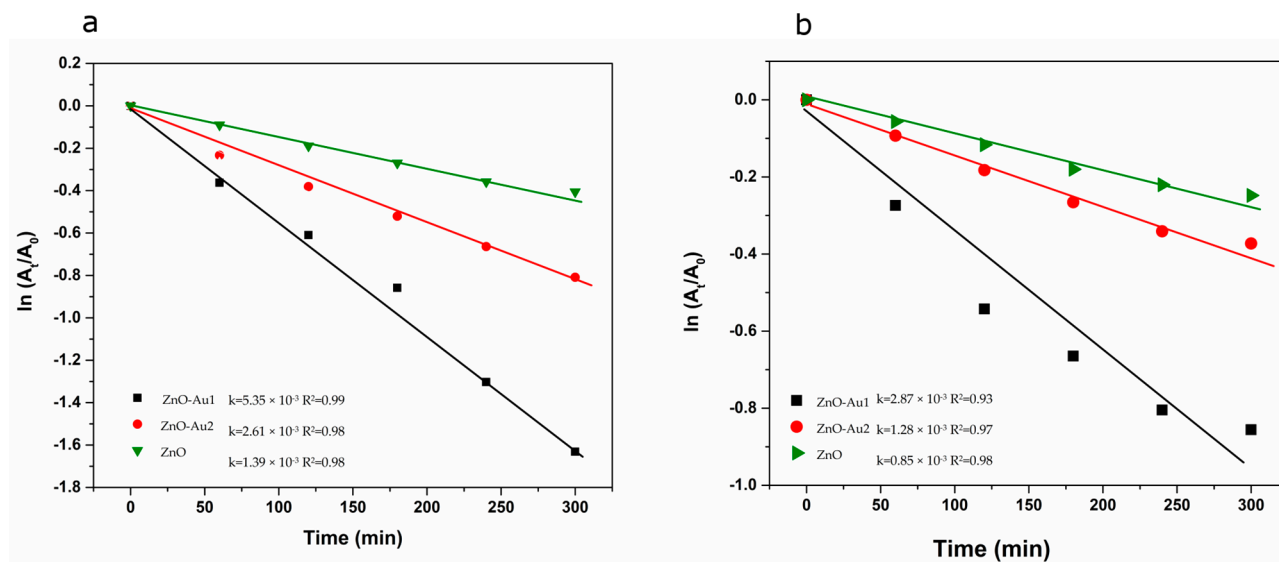


**Figure 12.** Evaluation of the photodegradation kinetic of (**a**) RhB and (**b**) OTC in the presence of ZnO nanoparticles, respectively, ZnO-Au1 and ZnO-Au2 nanocomposites.

Similar results have previously been reported in the scientific literature [39,59,60]. Some differences are present due to the fact that the efficiency of a photocatalyst depends on its composition, structure, porosity, and size, properties that are controlled by the synthesis method of the photocatalyst as well as the pollutant type and concentration. Thus, Lu et al. [60] obtained Au/ZnO nanorods using the hydrothermal method at 80 °C and employed them in methyl orange dye (5 mg/L) degradation. Morphology-related phenomena, such as photo-corrosion, were produced along the c-axes of pure ZnO nanorods, while Au decoration inhibited the occurrence of photo-corrosion and improved the photocatalytic activity. In addition, the same synthesis method led to the fabrication of honeycomb and porous cylindrical Au-ZnO heterostructures [39]. The photocatalytic performance, in terms of the degradation of rhodamine B (RhB), was approximately 90% under 200–1100 nm irradiation [61]. The high photocatalytic efficiency, even after 30 min, as evidenced in the above studies, was mainly due to the morphology of the nanoparticles, as well as to the composition and amounts of photocatalyst and pollutant that were used in the experiments.

In our experimental conditions, the small amount of photocatalyst (6 mg), as well as the low concentration of the pollutant ($1.0 \times 10^{-5}$ mol/L), may have contributed to the long duration of the photocatalytic process.

## 2.3. Reutilization Tests

A motivating property of ZnO-based photocatalysts is their ability to be reused several times following the first degradation of a specific pollutant. The recyclability of the ZnO-Au1 sample was tested here for both pollutants by four consecutive uses. For every experimental protocol, the ZnO-Au1 sample was washed with water and ethylene, then dried for 12 h. The photocatalytic activity obtained for each of the four tests is given in Figure 13 for both the RhB and OTC pollutants. The stability of the photocatalyst was demonstrated by the efficiency of the removal rate, even after four successive measurements.
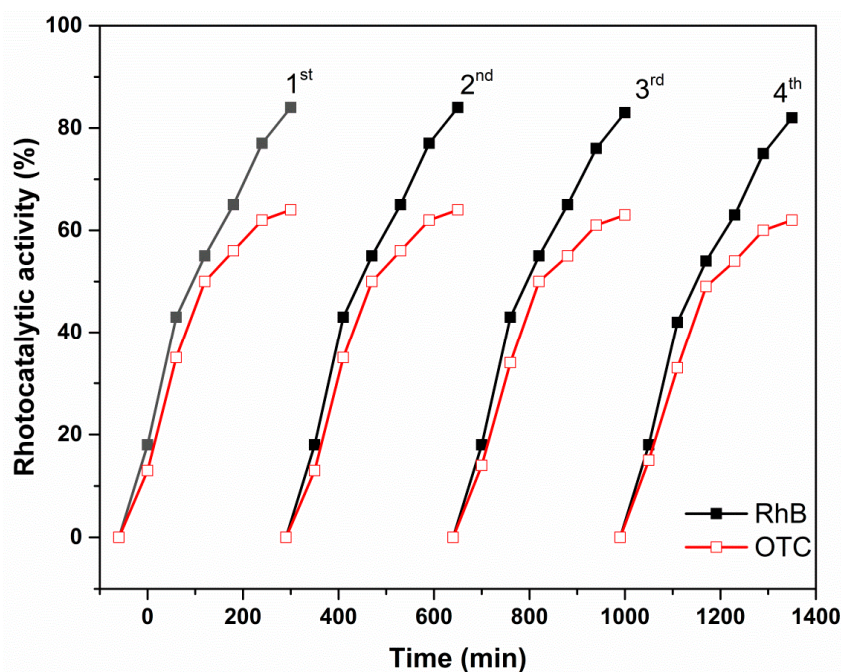
**Figure 13.** Photocatalyst stability test of the ZnO-Au1 nanocomposites for the photodegradation of RhB and OTC.

## 2.4. Generation of Reactive Oxygen Species

Electron spin resonance (ESR) investigations, coupled with the spin-trapping technique, were further employed to demonstrate the generation of ROS. The ZnO-Au1 sample was tested due to its increased photocatalytic capacity. The ZnO-Au1 dispersed in DMSO was illumined with visible light for 30 min, then further placed into the resonator of the ESR spectrometer. Figure 14 presents the resulting experimental and simulated spectra. In order to be able to assign the spin adducts observed in the complex experimental spectrum, which showed multiple peaks corresponding to various spin adducts produced during the irradiation, the simulated spectrum was calculated.
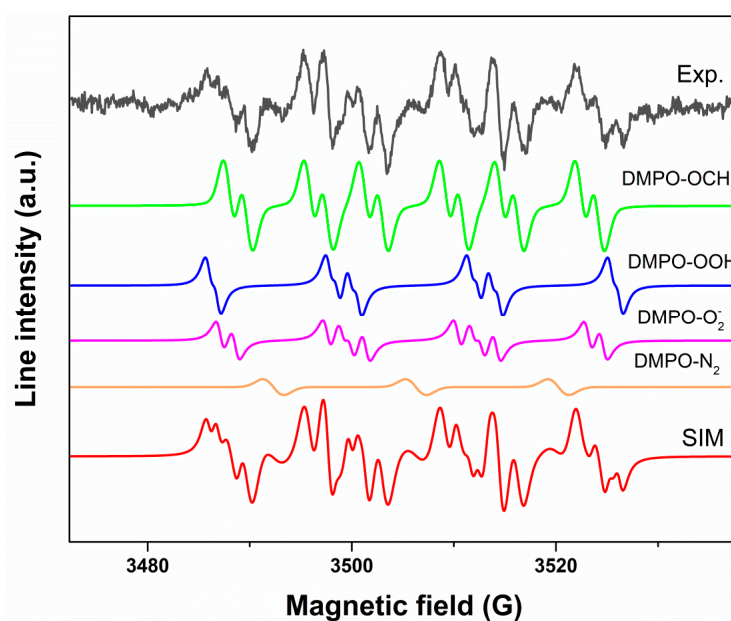


**Figure 14.** Experimental and simulated spectra of DMPO spin adducts generated by the ZnO-Au1 sample after 25 min of visible irradiation.

The simulated spectrum was obtained by performing a linear combination of the following spin adducts: •DMPO-OCH$_3$ (a$_N$ = 13.2 G, a$_H{}^\beta$ = 7.88 G, a$_H{}^\gamma$ = 1.6 G, g = 2.00976, relative concentration 52%), •DMPO-OOH (a$_N$ = 13.8 G, a$_H{}^\beta$ = 11.7 G, a$_H{}^\gamma$ = 0.8 G, g = 2.00976, relative concentration 23%), superoxide •DMPO-O$_2{}^-$ (a$_N$ = 12.79 G, a$_H{}^\beta$ = 10.45 G, a$_H{}^\gamma$ = 1.44 G, g = 2.00976, relative concentration 22%), and nitroxide-like radical (a$_N$ = 13.92 G, g = 2.00976, relative concentration 3%). In our specific experimental conditions, the cleavage of the DMPO molecule generated nitroxide-like radicals [62]. In addition, the •DMPO-OCH$_3$ adduct spin resulted from the interaction between the DMSO solvent and the •OH radical. From the simulation results, we can conclude that the ZnO-Au1 sample generated both hydroxyl radicals and superoxide anions with the capacity to degrade organic molecules in almost equal quantities.

To assess the active species involved in the degradation of RhB molecules, scavengers' tests were performed. Two scavengers were used: vitamin C for O$_2{}^{\bullet-}$ and isopropyl alcohol (IPA). The degradation rate after the addition of the scavengers (5 mM) into the pollutant solution was determined and compared with that obtained without their use. The results are presented in Figure 15. A decrease in photocatalytic activity was observed in the presence of both scavengers, the decrease being more pronounced in the case of IPA addition. The behavior was similar for both pollutants. These results demonstrate that both species were involved in pollutant degradation, but •OH radicals played a major role in the photodegradation process.
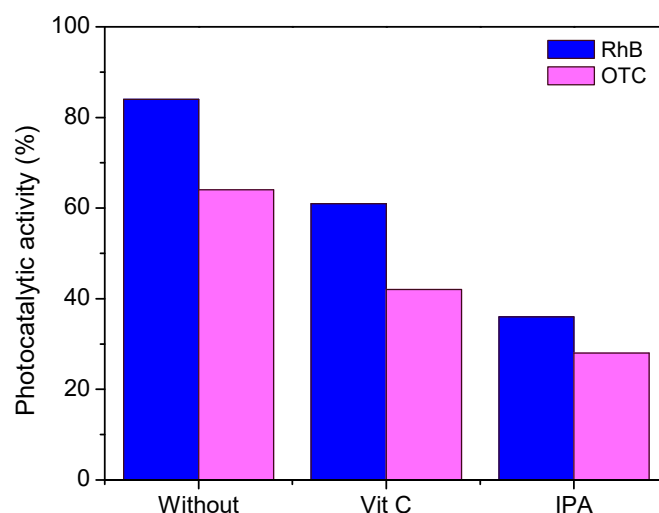


**Figure 15.** The effect of scavengers on the RhB and OTC photodegradation.

### 2.5. Photocatalytic Mechanism

Considering a semiconductor photocatalyst, the main stage in the photocatalytic degradation of organic pollutants includes the following steps: (i) photogeneration of charge carriers (e$^-$/h$^+$ pairs) under specific irradiation, (ii) the migration of charge carriers on the photocatalyst's surface/interface, and (iii) the redox reaction on the photocatalyst's surface with water molecules from RhB or OTC solutions.

The photocatalytic mechanism is governed by the behavior of photogenerated species. In order to interact with organic molecules, the e$^-$/h$^+$ pairs must possess sufficient lifetimes to form ROS, such as •O$_2{}^-$ and •OH, as indicated by the EPR spin trapping experiments. The immediate recombination of charge carriers leads to a decrease in photocatalytic performance, while radiative emissions increase. This behavior was evidenced by fluorescence emission spectra (Figure 8), where the sample with the best photocatalytic performance possessed poor emission properties. Generally, the defect states influence the photocatalytic activity. They can play the role of both of recombination center and separator of photogenerated charges, depending on their concentration. In our case, as the EPR results show, the ZnO nanoparticles have a high concentration of core and shell defects, which probably act

as recombination centers [1,63]. In the case of the ZnO-Au nanocomposites, the modulation of the photocatalytic activity depending on the amount of Au can be explained by trapping excitation electrons in the Au nanoparticles. Generally, in ZnO semiconductors, the Fermi level lies between the valence band and the conduction band, and is supposed to be higher than the Au work function. When the ZnO and Au form a heterojunction, the Fermi level of the new nanocomposite is moved closer to the conduction band, where the electrons are easily transferred from ZnO to Au under light excitation. Thus, the recombination of electrons excited in ZnO decreases, promoting the separation of $e^-/h^+$ along with formation of ROS, as well as increasing the photocatalytic activity. On the other hand, when the amount of Au increases, the excess electrons attract the holes and recombine, leading to a decrease in photocatalytic activity. To understand the photocatalytic process mediated by ZnO-Au nanocomposites, a band diagram is presented in Figure 16.
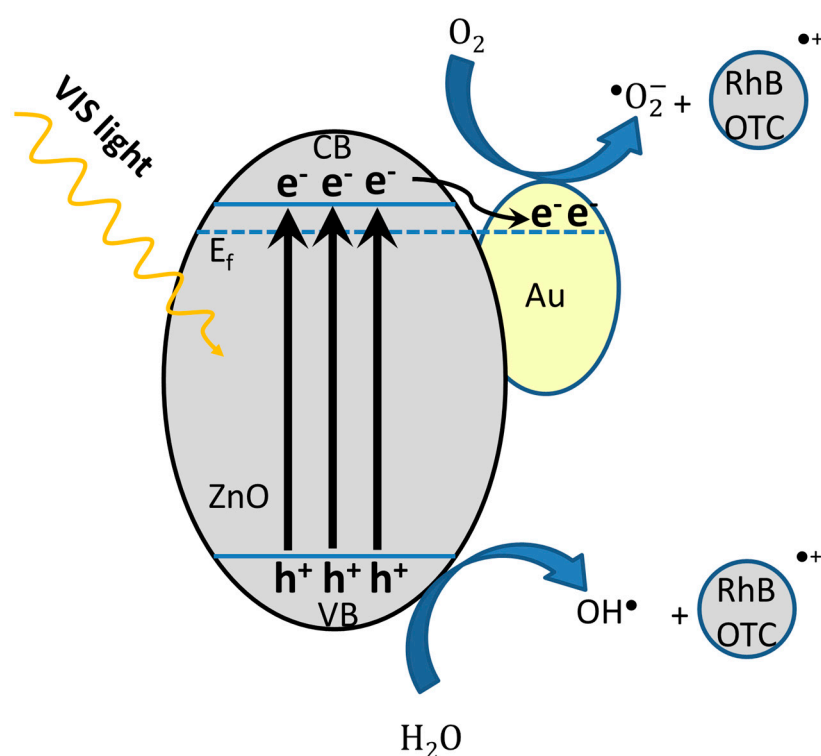


**Figure 16.** Schematic illustration of the photocatalytic mechanism depending on the behavior of the charge carriers.

## 3. Materials and Methods

### 3.1. Materials

All chemicals were of analytical grade and used as purchased, without any further purification. For the synthesis of ZnO-Au nanocomposites, the following reagents were used: zinc acetate- $Zn(CH_3COO)_2$ $2H_2O$ (Alpha Aesar, Bio Aqua Group, Targu Mures, Romania), sodium hydroxide-NaOH (Alpha Aesar, Bio Aqua Group, Targu Mures, Romania), absolute ethanol $C_2H_5OH$-EtOH (Sigma-Aldrich, Merck, KGaA, Darmstadt, Germany), oleic acid (VWR Chemicals, Lutterworth, Leicestershire, UK), oleylamine (Alpha Aesar, Bio Aqua Group, Targu Mures, Romania), hydrogen tetrachloroaurate trihydrate- $HAuCl_4 \cdot 3H_2O$ (Alpha Aesar, Bio Aqua Group, Targu Mures, Romania), and hydrazine hydrate $-NH_2$-$NH_2 \cdot H_2O$ (Sigma-Aldrich, Merck, KGaA, Darmstadt, Germany). In order to demonstrate the ROS production, 5,5-dimethyl-1-pyrroline N-oxide (DMPO) and dimethylformamide (DMF) were purchased from Sigma-Aldrich, Merck, KGaA, Darmstadt, Germany, and dimethyl sulfoxide (DMSO; >99.9%) was obtained from VWR Chemicals (Lutterworth, Leicestershire, UK). Rhodamine B (RhB) and oxytetracicline (OTC), used as recalcitrant pollutant, were purchased from Sigma-Aldrich, Merck, KGaA, Darmstadt, Germany. For

scavenger tests, two scavengers were used: vitamin C (Sigma-Aldrich, Merck, KGaA, Darmstadt, Germany) for $O_2^{\bullet-}$ and isopropyl alcohol (IPA) (Alpha Aesar, Bio Aqua Group, Targu Mures, Romania). The aqueous solutions were prepared using Milli-Q water with the Direct-Q 3UV system (Millipore, Bedford, MA, USA).

### 3.2. Synthesis of ZnO-Au Nanocomposites

To obtain ZnO-Au nanocomposites, $Zn(CH_3COO)_2 \times 2H_2O$, as the zinc source, was dissolved in 100 mL of $H_2O$ under continuous stirring, followed by sonication for half an hour. After that, 4M NaOH was added at a constant dropwise rate. The obtained precipitate was stirred for 2 h at 80 °C. The precipitate was centrifuged and washed five times with a water/ethanol mixture (1/1 *v/v*). The chemical precipitation procedure was also described in other articles, along with changes regarding the concentration of the reactants and the temperature [64].

Furthermore, ZnO nanoparticles were sonicated in 10 mL of water for 30 min, after which $10^{-2}$ mol/L of $HAuCl_4$ solution was added to the mixture under continuous stirring for another 2 h as follows: 110 mL (ZnOAu1) and 150 mL (ZnOAu2). After this step, the $HAuCl_4$ adsorbed on the ZnO precipitate was separated by centrifugation and washed with double-distilled water. The molar ratio ZnO:$HAuCl_4$ was 1:3 (ZnO-Au1) and 1:4 (ZnO-Au2). Then, the product was redispersed in water by adding 0.2 mL of 1M hydrazine. The color of the solution changed from light brown to purple, suggesting that Au nanoparticles were deposited onto the surface of ZnO particles. The Au quantity was adjusted by changing the concentration of $HAuCl_4$. Finally, the ZnO-Au nanocomposites were washed with water to remove the unreacted products and dried at 65 °C in the oven.

### 3.3. Methods

The crystalline structure was investigated by XRD, recorded by Rigaku-SmartLab automated Multipurpose X-ray Diffractometer (Rigaku, Tokyo, Japan), which is described in [65].

TEM images were performed by scanning transmission electron microscopy (STEM) using a Hitachi HD2700 Electron Microscope (Hitachi, Tokyo, Japan), which is described in [65]. Energy-dispersive X-ray spectroscopy (EDS) and chemical mapping of the elements were achieved using a Dual EDX System (X-Max N100TLE Silicon Drift Detector SDD) (Oxford Instruments, Oxford, UK) and AZtech software. The ZnO and ZnO-Au samples were dispersed using a BANDELIN SONOPLUS (Berlin, Germany).

The elemental composition analysis was performed by X-ray photoelectron spectroscopy (XPS) using a custom-build SPECS (Berlin, Germany) spectrometer working with an Al anode (1486.6 eV). CasaXPS software was used for analysis of the spectra. The intensities were calibrated with the corresponding relative sensitivity (RST), transmission (T), and electronic mean free path (MFP) factors. A value of 284.6 eV for the adventitious C 1s core-level line was considered for BE scale calibration.

The optical properties were evaluated using a double-beam JASCO-V570 UV-Vis spectrophotometer (JASCO Deutschland GmbH, Pfungstadt, Germany). Fluorescence emission and excitation spectra were measured using a JASCO FP-6500 spectrofluorometer (JASCO Deutschland GmbH, Pfungstadt, Germany) equipped with a Xe lamp of 150 W, 1800 lines/mm monochromator, and 1 nm spectral resolution.

To demonstrate the defects in the ZnO-Au nanocomposites, EPR measurements of powder samples were carried out on a Bruker E-500 ELEXSYS X-band (9.52 GHz) spectrometer (Rheinstetten, Baden-Württemberg, Germany) at room temperature. Using the EPR coupled with the spin trapping probe technique, we monitored the ROS production of ZnO and ZnO-Au in DMSO suspensions. This technique requires special solvents due to the instability of some radicals in water solutions. DMSO (dimethyl sulfoxide) was used as a solvent to prepare sample suspensions, and 5,5-dimethyl-1-pyrroline *N*-oxide (DMPO) was used as spin trapping agent. The samples were prepared by dispersing 10 mg of ZnO-Au in 1 mL of DMSO. Before being investigated, these suspensions were sonicated for 30 s.

The DMPO concentration was 0.2 M. The experimental and simulated spectra of ZnO-Au samples were prepared immediately before measurements, then transferred into a quartz flat cell optimized for liquid measurements.

The thermal behavior of the samples was investigated by thermogravimetric (TG) and differential thermal analysis (DTA) with a Metttler Toledo TGA/ SDTA851 instrument in platinum crucible, with a heating rate of 10 °C/min under a nitrogen flow of 30 mL/min.

The photocatalytic response was carried out in a Laboratory-Visible-Reactor system using a 400 W halogen lamp (Osram) and an ultrasonic bath. The catalyst (6 mg) was mixed into a 10 mL aqueous solution of RhB ($1.0 \times 10^{-5}$ mol/L) or oxytetracycline (50 mg/L); then, the obtained dispersion was stirred in the dark for 1 h to reach the adsorption equilibrium on the catalyst surface. Each degradation experiment was continuously conducted for 3 h. About 3.5 mL was extracted every 60 min, the catalyst was separated from the pollutant solution by centrifugation, and the pollutant concentration was determined by recording the absorption spectrum with an UV-Vis spectrophotometer (T90+; PG Instruments, Leicestershire, UK) by recording the pollutants' specific maximum absorbance. The volume of degraded solution was often used at the laboratory level, as can be seen in previous papers [66,67].

The photocatalytic activity was calculated using the following Equation (5):

$$\text{Photocatalytic activity} = \frac{A_0 - A_t}{A_0} \times 100, \tag{5}$$

where $A_0$ and $A_t$ represent the initial absorbance and that at time $t$, respectively.

The first-order kinetic model was used to describe the photocatalytic process (Equation (6)):

$$-ln\left(\frac{A_t}{A_0^*}\right) = k_i t, \tag{6}$$

where $A_t$ represents the absorbance of RhB at time $t$, $A_0^*$ the absorbance of RhB after dark adsorption, and $k_i$ the apparent kinetic constant.

## 4. Conclusions

In this paper, we report on the formation of ZnO-Au nanocomposites by using two-step liquid-phase chemical methods: chemical precipitation in order to obtain the ZnO nanoparticles, followed by reducing tetrachloroauric acid in the presence of hydrazine to obtain Au-decorated ZnO nanocomposites. The XRD diffraction of the synthesized ZnO-Au nanocomposites showed ZnO nanoparticles with hexagonal structures, together with the cubic structure of quasi-sphered Au nanoparticles less than 10 nm in size.

The UV-Vis absorption spectra confirmed the presence of Au nanoparticles on the nanosurface of ZnO through the development of a localized surface plasmon band, present around 575 nm. The Au decoration resulted in quenching of the near-band edge and visible emission of ZnO. The presence of core and shell defects in ZnO nanoparticles was determined using EPR spectroscopy. The amount of these defects is dependent on the Au content. The ability of ZnO-Au nanocomposites to serve as photocatalysts was investigated by the degradation of RhB and OTC pollutants. All samples showed photocatalytic activity, and the presence of Au nanoparticles enhanced the efficiency of the photocatalysts. At the interface between Au and ZnO nanoparticles, competitive processes occurred between local surface plasmons and exciton transitions in ZnO, with impact on the photocatalytic performance.

As indicated in fluorescence spectra, the sample with the best photocatalytic performance possessed poor emission properties. The defects acted as both charge traps and adsorption sites, tailoring the e$^-$/h$^+$ recombination. Our data show that ZnO-Au nanocomposites can be used as stable photocatalysts with excellent reusability and possible industrial applications. This research will be continued in order to establish the optimum ratio between the two components, ZnO and Au, with the aim of modulating the photocatalytic response. The ZnO-Au nanocomposites developed herein presented highly

improved photocatalytic activity, even at low photocatalyst and pollutant concentrations, making them very useful in technological processes.

## References

1. Yao, C.; Lin, J.; Li, L.; Jiang, K.; Hu, Z.; Xu, N.; Sun, J.; Wu, J. Au-Decorated ZnO Nanorod Powder and Its Application in Photodegradation of Organic Pollutants in the Visible Region. *Phys. Status Solidi A Appl. Mat. Sci.* **2021**, *218*, 2000737. [CrossRef]
2. Yao, C.; Chen, W.; Li, L.; Jiang, K.; Hu, Z.; Lina, J.; Xu, N.; Sun, J.; Wu, J. ZnO:Au nanocomposites with high photocatalytic activity prepared by liquid-phase pulsed laser ablation. *Opt. Laser Technol.* **2021**, *133*, 106533. [CrossRef]
3. Peralta, M.D.L.R.; Pal, U.; Zeferino, R.S. Photoluminescence (PL) Quenching and Enhanced Photocatalytic Activity of Au-Decorated ZnO Nanorods Fabricated through Microwave-Assisted Chemical Synthesis. *ACS Appl. Mater. Interfaces* **2012**, *4*, 4807–4816. [CrossRef] [PubMed]
4. Das, T.K.; Remanan, S.; Ghosh, S.; Ghosh, S.K.; Das, N.C. Efficient synthesis of catalytic active silver nanoparticles illuminated cerium oxide nanotube: A mussel inspired approach. *Environ. Nanotechnol. Monit. Manag.* **2021**, *15*, 100411. [CrossRef]
5. Lux, K.C.; Hot, J.; Fau, P.; Bertron, A.; Kahn, M.L.; Ringot, E.; Fajerwerg, K. Nano-gold decorated ZnO: An alternative photocatalyst promising for NOx degradation. *Chem. Eng. Sci.* **2023**, *267*, 118377. [CrossRef]
6. Zhu, Z.; Xia, H.; Li, H.; Han, S. Facile Construction of $Bi_2Sn_2O_7/g-C_3N_4$ Heterojunction with Enhanced Photocatalytic Degradation of Norfloxacin. *Inorganics* **2022**, *10*, 131. [CrossRef]
7. Das, T.K.; Ghosh, S.K.; Das, N.C. Green synthesis of a reduced graphene oxide/silver nanoparticles-based catalyst for degradation of a wide range of organic pollutants. *Nano-Struct. Nano-Objects* **2023**, *34*, 100960. [CrossRef]
8. Sharma, A.; Ahmad, J.; Flora, S.J.S. Application of advanced oxidation processes and toxicity assessment of transformation products. *Environ. Res.* **2018**, *167*, 223–233. [CrossRef]
9. Goktas, S.; Goktas, A. A comparative study on recent progress in efficient ZnO based nanocomposite and heterojunction photocatalysts: A review. *J. Alloy. Compd.* **2021**, *863*, 158734. [CrossRef]
10. Mardosaitė, R.; Jurkevičiūtė, A.; Račkauskas, S. Superhydrophobic ZnO Nanowires: Wettability Mechanisms and Functional Applications. *Cryst. Growth Des.* **2021**, *21*, 4765–4779. [CrossRef]
11. Manzano, C.V.; Philippe, L.; Serrà, A. Recent progress in the electrochemical deposition of ZnO nanowires: Synthesis approaches and applications. *Crit. Rev. Solid State Mater. Sci.* **2021**, *47*, 772–805. [CrossRef]
12. Ajimsha, R.S.; Mahapatra, A.; Das, A.K.; Sahu, V.K.; Misra, P. High output power density owing to enhanced charge transfer in ZnO-based triboelectric nanogenerator. *Energy* **2023**, *263*, 125646. [CrossRef]
13. Deckenbach, D.; Jörg, J.; Schneider, A. 3D hierarchically porous nanoscale ZnO anode for high-energy rechargeable zinc-air batteries. *J. Power Sources* **2021**, *488*, 229393. [CrossRef]
14. Kang, Y.; Yu, F.; Zhang, L.; Wang, W.; Chen, L.; Li, Y. Review of ZnO-based nanomaterials in gas sensors. *Solid State Ionics* **2021**, *360*, 115544. [CrossRef]
15. Vandarkuzhali, S.A.A.; Pugazhenthiran, N.; Mangalaraja, R.V.; Sathishkumar, P.; Viswanathan, B.; Anandan, S. Ultrasmall Plasmonic Nanoparticles Decorated Hierarchical Mesoporous $TiO_2$ as an Efficient Photocatalyst for Photocatalytic Degradation of Textile Dyes. *ACS Omega* **2018**, *3*, 9834–9845. [CrossRef]
16. Puspasari, V.; Ridhova, A.; Hermawan, A.; Amal, M.I.; Khan, M.M. ZnO-based antimicrobial coatings for biomedical applications. *Bioprocess Biosyst. Eng.* **2022**, *45*, 1421–1445. [CrossRef] [PubMed]
17. Cartwright, A.; Jackson, K.; Morgan, C.; Anderson, A.J.; Britt, D.W. A review of metal and metal-oxide nanoparticle coating technologies to inhibit agglomeration and increase bioactivity for agricultural applications. *Agronomyc* **2020**, *10*, 1018. [CrossRef]
18. Van der Bruggen, B. Sustainable implementation of innovative technologies for water purification. *Nat. Rev. Chem.* **2021**, *5*, 217–218. [CrossRef]
19. Allegretti, G.; Montoya, M.A.; Talamini, E. Assessing sectoral water stress states from the demand-side perspective through water footprint dimensions decomposition. *Sci. Total. Environ.* **2022**, *809*, 152216. [CrossRef]
20. Petrie, B.; Barden, R.; Kasprzyk-Hordern, B. A review on emerging contaminants in wastewaters and the environment: Current knowledge, understudied areas and recommendations for future monitoring. *Water Res.* **2015**, *72*, 3–27. [CrossRef]

21. Boczkaj, G.; Fernandes, A. Wastewater treatment by means of advanced oxidation processes at basic pH conditions: A review. *Chem. Eng. J.* **2017**, *320*, 608–633. [CrossRef]

22. Li, C.; Tian, Q.; Zhang, Y.; Li, Y.; Yang, X.; Zheng, H.; Chen, L.; Li, F. Sequential combination of photocatalysis and microalgae technology for promoting the degradation and detoxification of typical antibiotics. *Water Res.* **2022**, *210*, 117985. [CrossRef]

23. Cai, G.; Liu, T.; Zhang, J.; Song, H.; Jiang, Q.; Zhou, C. Control for chlorine resistant spore forming bacteria by the coupling of pre-oxidation and coagulation sedimentation, and UV-AOPs enhanced inactivation in drinking water treatment. *Water Res.* **2022**, *219*, 118540. [CrossRef]

24. Yu, M.; Wang, J.; Tang, L.; Feng, C.; Liu, H.; Zhang, H.; Peng, B.; Chen, Z.; Xie, Q. Intimate coupling of photocatalysis and biodegradation for wastewater treatment: Mechanisms, recent advances and environmental applications. *Water Res.* **2020**, *175*, 115673. [CrossRef]

25. Wang, J.; Wang, G.; Jiang, J.; Wan, Z.; Su, Y.; Tang, H. Insight into charge carrier separation and solar-light utilization: rGO decorated 3D ZnO hollow microspheres for enhanced photocatalytic hydrogen evolution. *J. Colloid Interface Sci.* **2020**, *564*, 322–332. [CrossRef]

26. Wang, Y.J.; Wang, F.M.; He, J. Controlled fabrication and photocatalytic properties of a three-dimensional ZnO nanowire/reduced graphene oxide/CdS heterostructure on carbon cloth. *Nanoscale* **2013**, *5*, 11291–11297. [CrossRef]

27. Abarna, B.; Preethi, T.; Karunanithi, A.; Rajarajeswari, G.R. Influence of jute template on the surface, optical and photocatalytic properties of sol-gel derived mesoporous zinc oxide. *Mater. Sci. Semicond. Process.* **2016**, *56*, 243–250. [CrossRef]

28. Sun, X.; Luo, X.; Zhang, X.; Xie, J.; Jin, S.; Wang, H.; Zheng, X.-S.; Wu, X.; Xie, Y. Enhanced Superoxide Generation on Defective Surfaces for Selective Photooxidation. *J. Am. Chem. Soc.* **2019**, *141*, 3797–3801. [CrossRef] [PubMed]

29. Singh, J.; Soni, R.K. Controlled synthesis of CuO decorated defect enriched ZnO nanoflakes for improved sunlight-induced photocatalytic degradation of organic pollutants. *Appl. Surf. Sci.* **2020**, *521*, 146420. [CrossRef]

30. Toe, M.Z.; Pung, S.-Y.; Le, A.T.; Yaccob, K.A.B.; Matsuda, A.; Tan, W.K.; Han, S.S. Morphology and optical properties of ZnO nanorods coupled with metal oxides of various bandgaps by photo-oxidation. *J. Lumin* **2021**, *229*, 117649. [CrossRef]

31. Azar, B.E.; Ramazani, A.; Fardood, S.T.; Morsali, A. Green synthesis and characterization of ZnAl$_2$O$_4$@ZnO nanocomposite and its environmental applications in rapid dye degradation. *Optik* **2020**, *208*, 164129. [CrossRef]

32. Ahmed, M.A.; Abou-Gamra, Z.M.; Alshakhanbeh, M.A.; Medien, H. Control Synthesis of Metallic Gold Nanoparticles Homogeneously Distributed on Hexagonal ZnO Nanoparticles for Pho-tocatalytic Degradation of Methylene Blue Dye. *Environ. Nanotechnol. Monit. Manag.* **2019**, *12*, 100217. [CrossRef]

33. He, W.; Kim, H.-K.; Wamer, W.G.; Melka, D.; Callahan, J.H.; Yin, J.-J. Photogenerated charge carriers and reactive oxygen species in ZnO/Au hybrid nanostructures with enhanced photo-catalytic and antibacterial activity. *J. Am. Chem. Soc.* **2014**, *136*, 750–757. [CrossRef]

34. Macias-Montero, M.; Pelaez, R.J.; Rico, V.J.; Saghi, Z.; Midgley, P.; Afonso, C.N.; Gonzalez-Elipe, A.R.; Borras, A. Laser treatment of Ag@ZnO nanorods as longlife-span SERS surfaces. *ACS Appl. Mater. Interfaces* **2015**, *7*, 2331–2339. [CrossRef] [PubMed]

35. Wu, S.-H.; Chan, C.-H.; Chien, C.-H.; Yaseen, M.T.; Liang, C.-T.; Chang, Y.-C. Enhanced Emission and Photoconductivity Due to Photo-Induced Charge Transfer from Au Nanoislands to ZnO. *Appl. Phys. Lett.* **2016**, *108*, 041104. [CrossRef]

36. Chamorro, W.; Ghanbaja, J.; Battie, Y.; Naciri, A.E.; Soldera, F.; Mücklich, F.; Horwat, D. Local Structure-Driven Localized Surface Plasmon Absorption and Enhanced Photoluminescence in ZnO-Au Thin Films. *J. Phys. Chem. C* **2016**, *120*, 29405–29413. [CrossRef]

37. Viter, R.; Balevicius, Z.; Abou Chaaya, A.; Baleviciute, I.; Tumenas, S.; Mikoliunaite, L.; Ramanavicius, A.; Gertnere, Z.; Zalesska, A.; Vataman, V.; et al. The Influence of Localized Plasmons on the Optical Properties of Au/ZnO Nanostructures. *J. Mat. Chem. C* **2015**, *3*, 6815–6821. [CrossRef]

38. Fageria, P.; Gangopadhyay, S.; Pande, S. Synthesis of ZnO/Au and ZnO/Ag nanoparticles and their photocatalytic application using UV and visible light. *RSC Adv.* **2014**, *4*, 294262. [CrossRef]

39. Yang, S.; Wang, L.; Yan, Y.; Yang, L.; Li, X.; Lu, Z.; Zhai, H.; Han, D.; Huo, P. Two Hybrid Au-ZnO Heterostructures with Different Hierarchical Structures: Towards Highly Efficient Photocatalysts. *Sci. Rep.* **2019**, *9*, 16863. [CrossRef]

40. Liu, L.; Yang, H.; Ren, X.; Tang, J.; Li, Y.; Zhang, X. Au-ZnO Janus Nanoparticles Exhibiting Strong Charge-Transfer-Induced SERS for Recyclable SERS-Active Substrates. *Nanoscale* **2015**, *7*, 5147–5151. [CrossRef]

41. Raji, R.; Gopchandran, K.G. Plasmonic photocatalytic activity of ZnO:Au nanostructures: Tailoring the plasmon absorption and interfacial charge transfer mechanism. *J. Hazard. Mater.* **2019**, *368*, 345–357. [CrossRef]

42. Georgiev, P.; Kaneva, N.; Bojinova, A.; Papazova, K.; Mircheva, K.; Balashev, K. Effect of gold nanoparticles on the photocatalytic efficiency of ZnO films. *Colloids Surf. A Physicochem. Eng. Asp.* **2014**, *460*, 240–247. [CrossRef]

43. Gebreslassie, G.; Gebrezgiabher, M.; Lin, B.; Thomas, M.; Linert, W. Direct Z-Scheme CoFe$_2$O$_4$-Loaded g-C$_3$N$_4$ Photocatalyst with High Degradation Efficiency of Methylene Blue under Visible-Light Irradiation. *Inorganics* **2023**, *11*, 119. [CrossRef]

44. Chebanenko, M.I.; Tikhanova, S.M.; Nevedomskiy, V.N.; Popkov, V.I. Synthesis and Structure of ZnO-Decorated Graphitic Carbon Nitride (g-C$_3$N$_4$) with Improved Photocatalytic Activity under Visible Light. *Inorganics* **2022**, *10*, 249. [CrossRef]

45. Gupta, N.K.; Gha, Y.; Kim, S.; Bae, J.; Kim, K.S. Photocatalytic Degradation of Organic Pollutants over MFe$_2$O$_4$ (M = Co, Ni, Cu, Zn) Nanoparticles at Neutral pH. *Sci. Rep.* **2020**, *10*, 4942. [CrossRef] [PubMed]

46. Toloman, D.; Stefan, M.; Macavei, S.; Barbu-Tudoran, L.; Popa, A. Photocatalytic Self-Cleaning PVDF Membrane Blended with MWCNT-ZnO Nanocomposites for RhB Removal. *Coatings* **2023**, *13*, 594. [CrossRef]

47.  Williamson, G.K.; Hall, W.H. X-ray Line Broadening from Filed Aluminium and Wolfram. *Acta Metall.* **1953**, *1*, 22–31. [CrossRef]
48.  Pana, O.; Teodorescu, C.M.; Chauvet, O.; Payen, C.; Macovei, D.; Turcu, R.; Soran, M.L.; Aldea, N.; Barbu, L. Structure, morphology and magnetic properties of Fe–Au core-shell nanoparticles. *Surf. Sci.* **2007**, *601*, 4352–4357. [CrossRef]
49.  Gogurla, N.; Sinha, A.K.; Santra, S.; Manna, S.; Ray, S.K. Multifunctional Au-ZnO plasmonic nanostructures for enhanced UV photodetector and room temperature NO sensing devices. *Sci. Rep.* **2014**, *4*, 6483. [CrossRef]
50.  Yao, C.; Lin, J.; Wu, L.; Li, L.; Xu, N.; Sun, J.; Wu, J. High-Visible-Light Photocatalytic Activity of ZnO–Au Nanocomposites Synthesized by a Controlled Hydrothermal Method. *Phys. Status Solidi A* **2021**, *218*, 2100150. [CrossRef]
51.  Shan, G.; Zhong, M.; Wang, S.; Li, Y.; Liu, Y. The synthesis and optical properties of the heterostructured ZnO/Au nanocomposites. *J. Colloid Interface Sci.* **2008**, *326*, 392–395. [CrossRef] [PubMed]
52.  Yang, J.; Zhao, X.; Shan, X.; Fan, H.; Yang, L.; Zhang, Y.; Li, X. Blue-shift of UV emission in ZnO/graphene composites. *J. Alloy. Compd.* **2013**, *556*, 1–5. [CrossRef]
53.  Vanheusden, K.; Warren, W.L.; Seager, C.H.; Tallant, D.R.; Voigt, J.A.; Gnade, B.E. Mechanisms behind green photoluminescence in ZnO phosphor powders. *J. Appl. Phys.* **1996**, *79*, 7983–7990. [CrossRef]
54.  Zhou, H.; Hofstaetter, A.; Hofmann, D.M.; Meyer, B.K. Magnetic resonance studies on ZnO nanocrystals. *Microelectron. Eng.* **2003**, *66*, 59–64. [CrossRef]
55.  Li, D.; Leung, Y.H.; Djurišić, A.B.; Liu, Z.T.; Xie, M.H.; Shi, S.L.; Xu, S.; Chan, W.K. Different origins of visible luminescence in ZnO nanostructures fabricated by the chemical and evaporation methods. *Appl. Phys. Lett.* **2004**, *85*, 1601–1603. [CrossRef]
56.  Kaftelen, H.; Ocakoglu, K.; Thomann, R.; Tu, S.; Weber, S.; Erdem, E. EPR and photoluminescence spectroscopy studies on the defect structure of ZnO nanocrystals. *Phys. Rev. B* **2012**, *86*, 014113. [CrossRef]
57.  Djurišić, A.B.; Choy, W.C.H.; Roy, V.A.L.; Leung, Y.H.; Kwong, C.Y.; Cheah, K.W.; Rao, T.K.G.; Chan, W.K.; Lui, H.F.; Surya, C. Photoluminescence and Electron Paramagnetic Resonance of ZnO Tetrapod Structures. *Adv. Funct. Mater.* **2004**, *14*, 856–864. [CrossRef]
58.  Toloman, D.; Pana, O.; Stefan, M.; Popa, A.; Leostean, C.; Macavei, S.; Silipas, D.; Perhaita, I.; Lazar, M.D.; Barbu-Tudoran, L. Photocatalytic activity of $SnO_2$-$TiO_2$ composite nanoparticles modified with PVP. *J. Colloid Interface Sci.* **2019**, *542*, 296–307. [CrossRef]
59.  Zhao, X.; Li, Z.; Yu, J.; Li, C.; Xu, S.; Li, F.; Zhang, C.; Man, B.; Zhang, C. Plasmonic and bi-piezoelectric enhanced photocatalysis using PVDF/ZnO/Au nanobrush. *Nanophotonics* **2022**, *11*, 3339–3349. [CrossRef]
60.  Lu, J.; Wang, H.; Peng, D.; Chen, T.; Dong, S.; Chang, Y. Synthesis and properties of Au/ZnO nanorods as a plasmonic photocatalyst. *Phys. E Low-Dimens. Syst. Nanostructures* **2016**, *78*, 41–48. [CrossRef]
61.  She, P.; Liu, Z.; Sun, H.; Shang, Y.; Li, Z.; Qin, Z.; Xu, K.; Yu, Z. Bio-inspired Spin-ach-leaf-based Au/ZnO Nanocomposites as Photocatalyst. *J. Bionic Eng.* **2019**, *16*, 1080–1091. [CrossRef]
62.  Diaz-Uribe, C.E.; Daza, M.C.; Martínez, F.; Páez-Mozo, E.A.; Guedes, C.L.B.; Di Mauro, E. Visible light superoxide radical anion generation by tetra(4-carboxyphenyl) porphyrin /$TiO_2$: EPR characterization. *J. Photochem. Photobiol. A* **2010**, *215*, 172. [CrossRef]
63.  Lee, Y.; Fujimoto, T.; Yamanaka, S.; Kuga, Y. Evaluation of photocatalysis of Au supported ZnO prepared by the spray pyrolysis method. *Adv. Powder Technol.* **2021**, *32*, 1619–1626. [CrossRef]
64.  Rapa, M.; Stefan, M.; Popa, A.; Toloman, D.; Leostean, C.; Borodi, G.; Vodnar, D.C.; Wrona, M.; Salafranca, J.; Nerin, C.; et al. Electrospun Nanosystems Based on PHBV and ZnO for Ecological Food Packaging. *Polymers* **2021**, *13*, 2123. [CrossRef]
65.  Falamas, A.; Marica, I.; Popa, A.; Toloman, D.; Pruneanu, S.; Pogacean, F.; Nekvapil, F.; Silipas, T.D.; Stefan, M. Size-dependent spectroscopic insight into the steady-state and time-resolved optical properties of ZnO photocatalysts. *Mater. Sci. Semicond. Process.* **2022**, *145*, 106644. [CrossRef]
66.  Madanu, T.L.; Mouchet, S.R.; Deparis, O.; Liu, J.; Li, Y.; Su, B.L. Tuning and transferring slow photons from $TiO_2$ photonic crystals to $BiVO_4$ nanoparticles for unprecedented visible light photoca-talysis. *J. Colloid Interf. Sci.* **2023**, *634*, 290–299. [CrossRef] [PubMed]
67.  Guo, X.; Zhu, H.; Li, Q. Visible-light-driven photocatalytic properties of ZnO/$ZnFe_2O_4$ core/shell nanocable arrays. *Appl. Catal. B Environ.* **2014**, *160–161*, 408–414. [CrossRef]